Supporting Information

Boosting Ethane/Ethylene Separation within Isoreticular Ultramicroporous Metal-Organic Frameworks

Rui-Biao Lin,[1] Hui Wu,[2] Libo Li,[1] Xiao-Liang Tang,[1] Zhiqiang Li,[1] Junkuo Gao,[1] Hui Cui,[1] Wei Zhou,[2] Banglin Chen*[1]*

[1]Department of Chemistry, University of Texas at San Antonio One UTSA Circle, San Antonio, Texas 78249-0698, USA Fax: (+1)210-458-7428, E-mail: banglin.chen@utsa.edu

[2]NIST Center for Neutron Research, National Institute of Standards and Technology, Gaithersburg, Maryland 20899-6102, USA, E-mail: wzhou@nist.gov

Adsorbate–adsorbent potential energy.[S1] For physical adsorption, the adsorbate–adsorbent potential is:

$$\phi = \phi_D + \phi_R + \phi_{Ind} + \phi_{F\mu} + \phi_{\dot{F}Q}$$

where ϕ_D is the dispersion energy, ϕ_R is the close-range repulsion energy, ϕ_{Ind} is the induction energy (interaction between electric field and an induced dipole), $\phi_{F\mu}$ is the interaction between electric field (F) and a permanent dipole (μ), $\phi_{\dot{F}Q}$ is interaction between field gradient ($\dot{F}$) and a quadrupole (with quadrupole moment Q).

In specific,

$$\phi_D = -\frac{\mathrm{A}}{r^6}$$

$$\phi_R = +\frac{\mathrm{B}}{r^{12}}$$

$$\phi_{Ind} = -\frac{1}{2}\alpha F^2 = -\frac{\alpha q^2}{2r^4(4\pi\in_0)^2}$$

$$\phi_{F\mu} = -F\mu\cos\theta = -\frac{q\mu\cos\theta}{r^2(4\pi\in_0)}$$

$$\phi_{\dot{F}Q} = \frac{1}{2}Q\dot{\mathrm{F}} = -\frac{Qq(3\cos^2\theta-1)}{4r^3(4\pi\in_0)}$$

where A and B are constants, α is the polarizability, F is the electric field, q is the electronic charge of ion on surface, $\in_0$ is the permittivity of a vacuum, μ is the permanent dipole moment, θ is the angle between the direction of the field or field gradient and the axis of the dipole or linear quadrupole, Q is linear quadrupole moment (+ or −). The important parameter, r, is the distance between the centers of the interacting pair.

Density-Functional Theory Calculations. First-principles density-functional theory (DFT) calculations were performed using the Quantum-Espresso package.[S2] A semi-empirical addition of dispersive forces to conventional DFT was included in the calculation to account for van der Waals interactions.[S3] We used Vanderbilt-type ultrasoft pseudopotentials and generalized gradient approximation (GGA) with Perdew−Burke−Ernzerhof (PBE) exchange correlation. A cutoff energy of 544 eV and a 2 × 2 × 2 *k*-point mesh (generated using the Monkhosrt-Pack scheme) were found to be enough for the total energy to converge within 0.01 meV/atom. We first optimized the structure of **Cu(Qc)$_2$**. Gas molecule was then introduced to the optimized host structure at the experimentally identified adsorption site, followed by a full structural relaxation. To obtain the gas binding energy, an isolated gas molecule placed in a supercell (with the same cell dimensions as the MOF crystal) was also relaxed as a reference. The static binding energy (at T = 0 K) was then calculated using: $E_B = E(\text{MOF}) + E(C_2H_x) - E(\text{MOF} + C_2H_x)$ (x = 4, 6).

Calculation of isosteric heat of adsorption (Q_{st}).

The Clausius-Clapeyron equation was employed to calculate the enthalpies of gas adsorption:

$$\frac{\partial(\ln P)}{\partial(1/T)} = -\frac{Q_{st}}{R}$$

Where P is the pressure, T is the temperature, R is the universal gas constant.

Its integrated form between two equilibrium states:

$$\ln\left(\frac{P_2}{P_1}\right) = \frac{Q_{\mathrm{st}}}{R}\left[\frac{1}{T_1} - \frac{1}{T_2}\right]$$

Where P_1 is the equilibrium pressure at temperature T_1, P_2 is the equilibrium pressure at temperature T_2.

IAST Calculation. In order to calculate the selective sorption performance of different MOFs toward the separation of binary mixed gases, the fitting of the single-component C_2H_6 and C_2H_4 adsorption isotherms was carried out based on the Langmuir-Freundlich or Langmuir model, depending on the coefficient of determination (R^2). Adsorption isotherms and gas selectivities of mixed C_2H_6/C_2H_4 (50/50, v/v) at 298 K for different MOFs were predicted using the ideal adsorbed solution theory (IAST).

Dual-site Langmuir-Freundlich (DSLF) model is listed as below:

$$N = N_1^{\max} \times \frac{b_1 p^{1/n1}}{1 + b_1 p^{1/n1}} + N_2^{\max} \times \frac{b_2 p^{1/n2}}{1 + b_2 p^{1/n2}}$$

Where p (unit: kPa) is the pressure of the bulk gas at equilibrium with the adsorbed phase, N (unit: mol/kg) is the adsorbed amount per mass of adsorbent, $N_1^{\max}$ and $N_2^{\max}$ (unit: mmol/g) are the saturation capacities of two different sites, b_1 and b_2 (unit: 1/kPa) are the affinity coefficients of these sites, and n_1 and n_2 represent the deviations from an ideal homogeneous surface. It should be noted that:

1) $N_2^{\max}$ =0, b_2 = 0 and $1/n_2$ =1, it is Langmuir-Freundlich model;
2) $1/n_1$ =1 and $1/n_2$ =1, it is dual-site Langmuir model;
3) $1/n_1$ =1, $N_2^{\max}$ =0, b_2 = 0 and $1/n_2$ =1, it is Langmuir model.

Breakthrough separation experiments and procedures

The breakthrough experiments were carried out in dynamic gas breakthrough set-up.[S4] A stainless steel column with inner dimensions of ϕ 4 × 150 mm was used for sample packing. Microcrystalline sample (1.037 g) with particle size of 220–320 μm obtained via sieving was then packed into the column. The mixed gas flow and pressure were controlled by using a pressure controller valve and a mass flow controller. Outlet effluent from the column was continuously monitored using gas chromatography (GC-2014, SHIMADZU) with a thermal conductivity detector (TCD). The column packed with sample was firstly purged with He flow (20 mL min^{-1}) for 0.5 h at room temperature. The mixed gas flow rate during breakthrough process is 2 mL min^{-1} using 50/50 (v/v) C_2H_6/C_2H_4. After the breakthrough experiment, the sample was regenerated under vacuum.

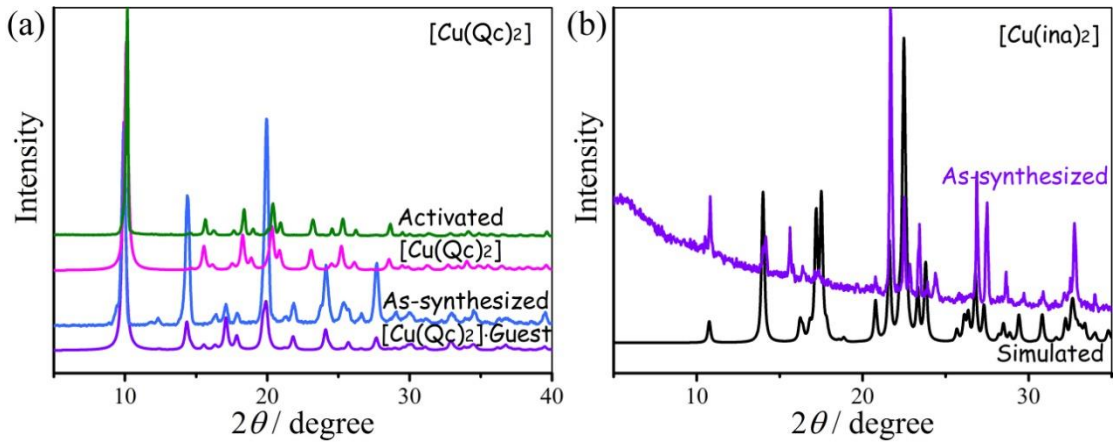

Figure S1. PXRD patterns of (a) **Cu(Qc)$_2$** and (b) **Cu(ina)$_2$**.

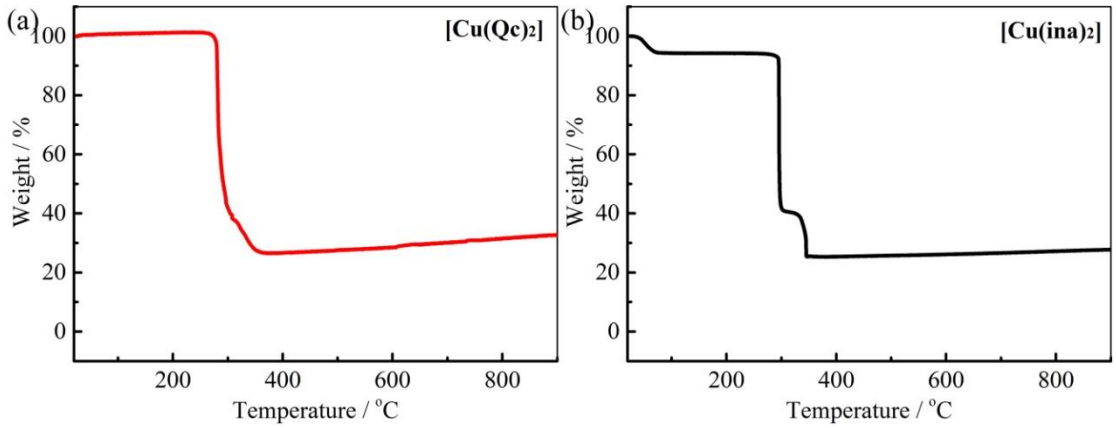

Figure S2. TGA curve of activated (a) **Cu(Qc)$_2$** and (b) **Cu(ina)$_2$** under an air atmosphere. For **Cu(ina)$_2$**, the initial slight weight loss can be attributed to gaseous impurity captured form the air.

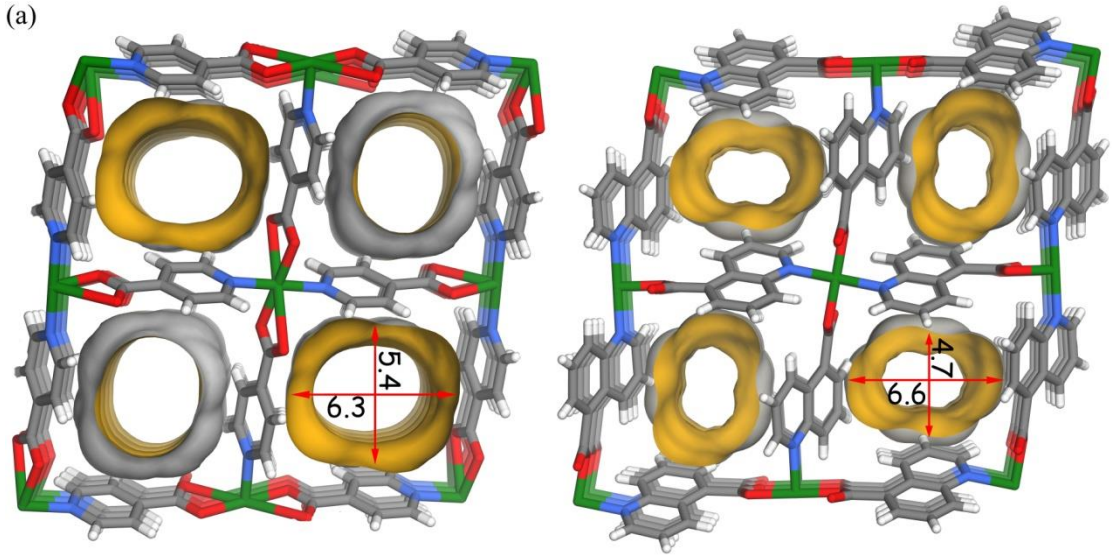

Figure S3. The pore channels in as-synthesized (a) **Cu(ina)$_2$** and (b) **Cu(Qc)$_2$** as viewed along crystallographic *a* axis (unit: Å).

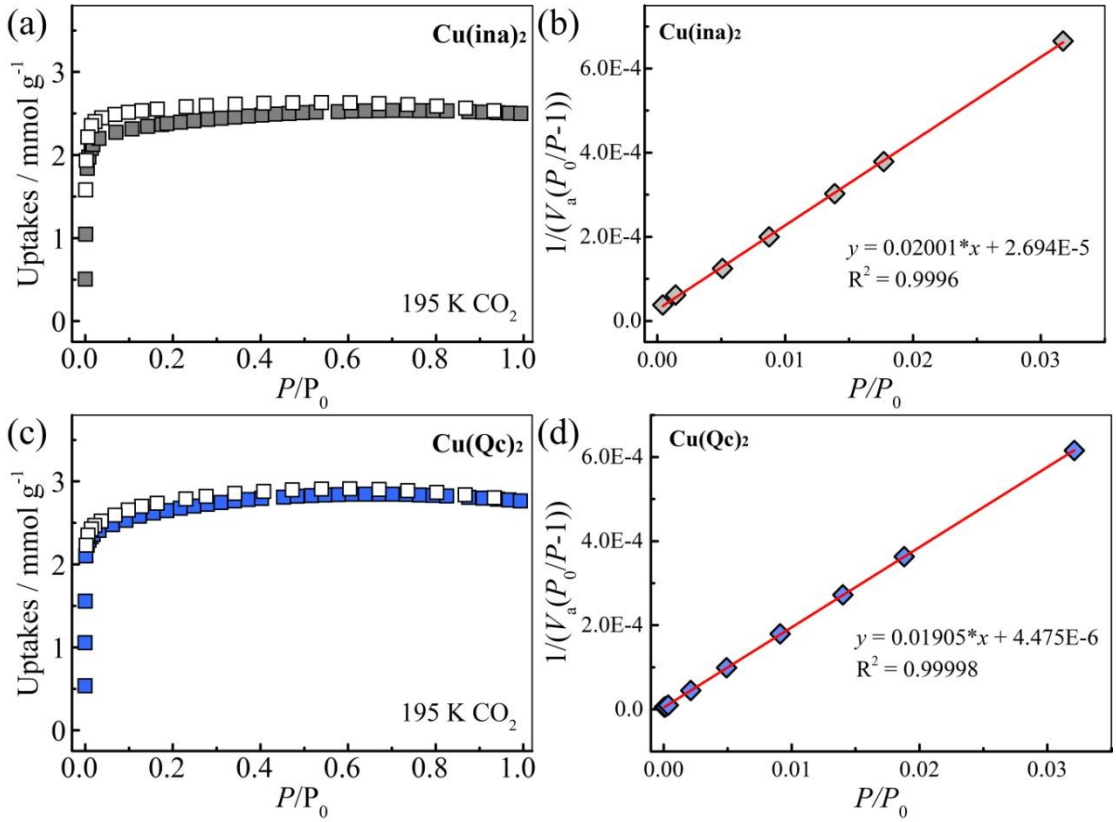

Figure S4. BET calculation for (a-b) **Cu(ina)$_2$** and (c-d) **Cu(Qc)$_2$** based on their corresponding CO_2 adsorption isotherms at 195 K.

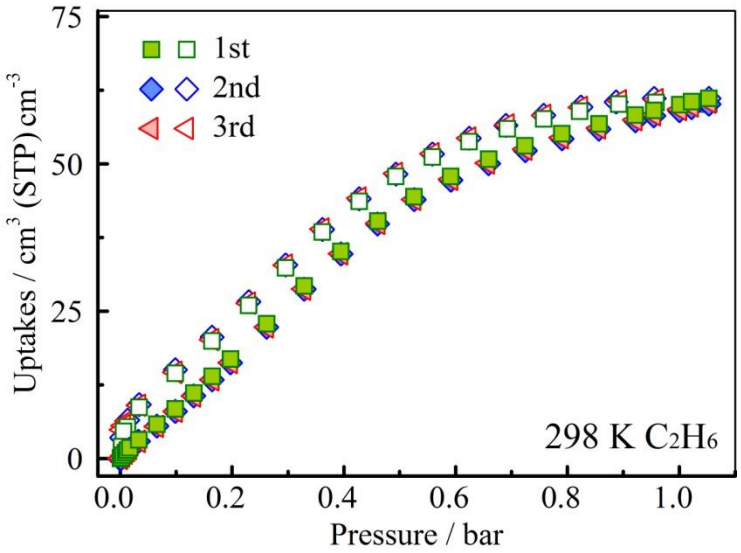

Figure S5. Multiple cycles of C_2H_6 sorption measurements for **[Cu(Qc)$_2$]** at 298 K.

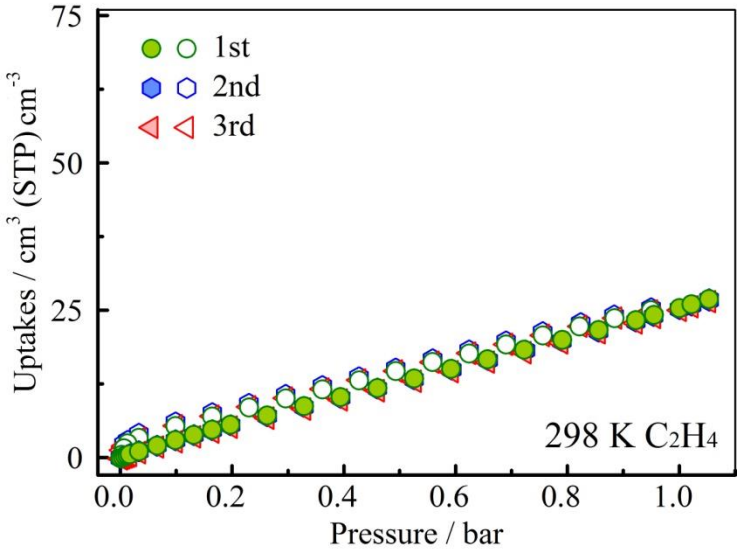

Figure S6. Multiple cycles of C_2H_4 sorption measurements for **[Cu(Qc)$_2$]** at 298 K.

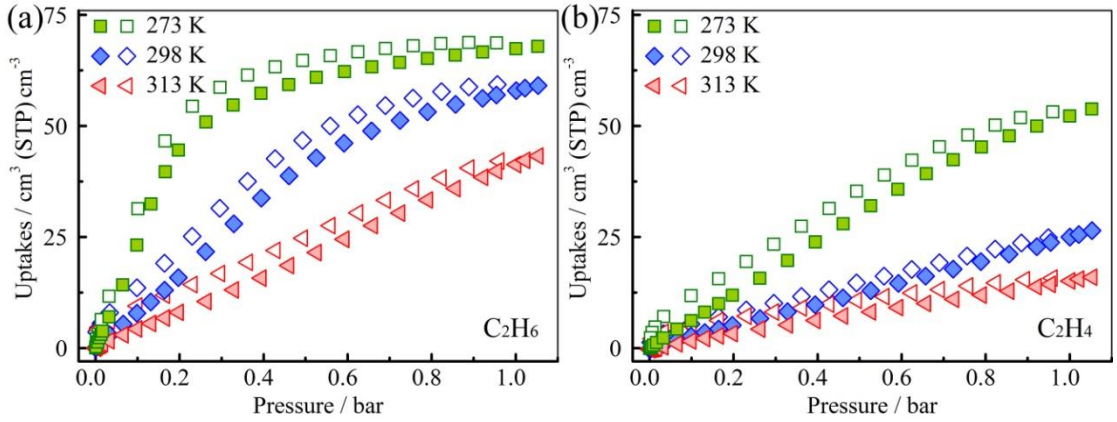

Figure S7. C_2H_6 and C_2H_4 sorption isotherms for **[Cu(Qc)$_2$]** at 273, 298 and 313 K.

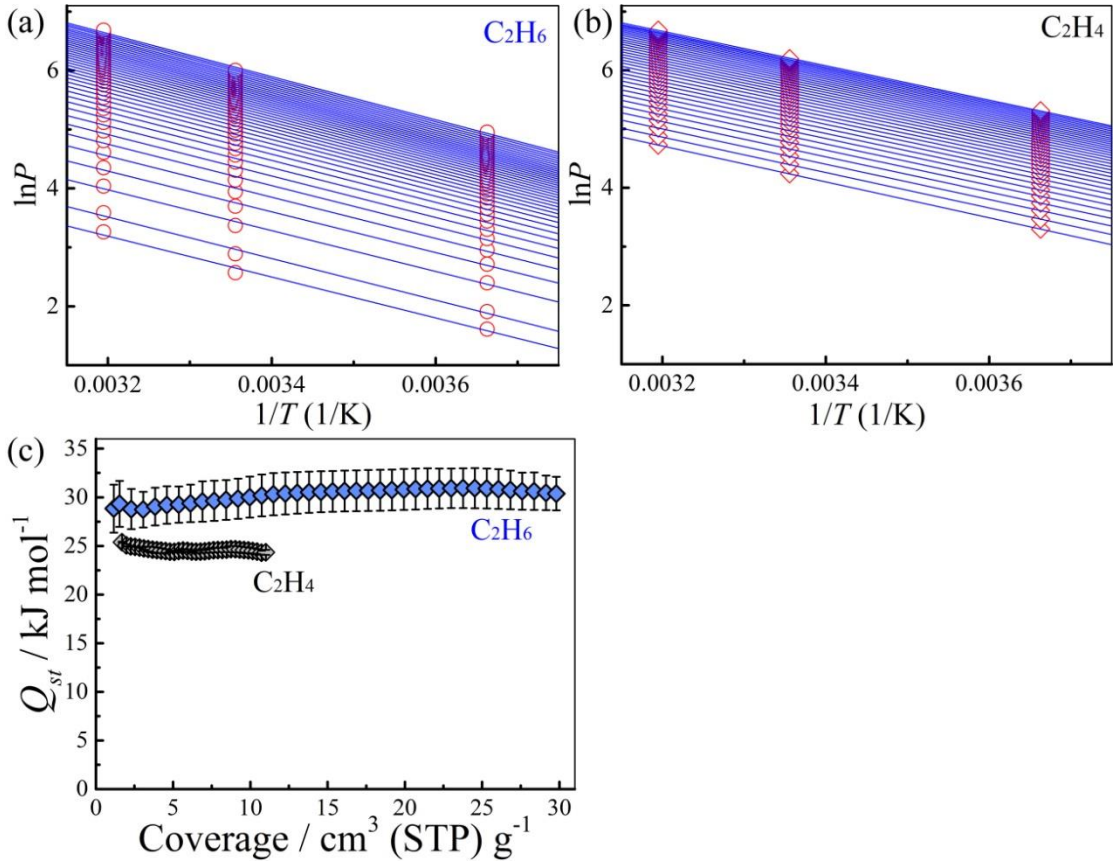

Figure S8. (a-b) Isostere plots and (c) corresponding adsorption enthalpies of **[Cu(Qc)$_2$]** for C_2H_6 and C_2H_4.

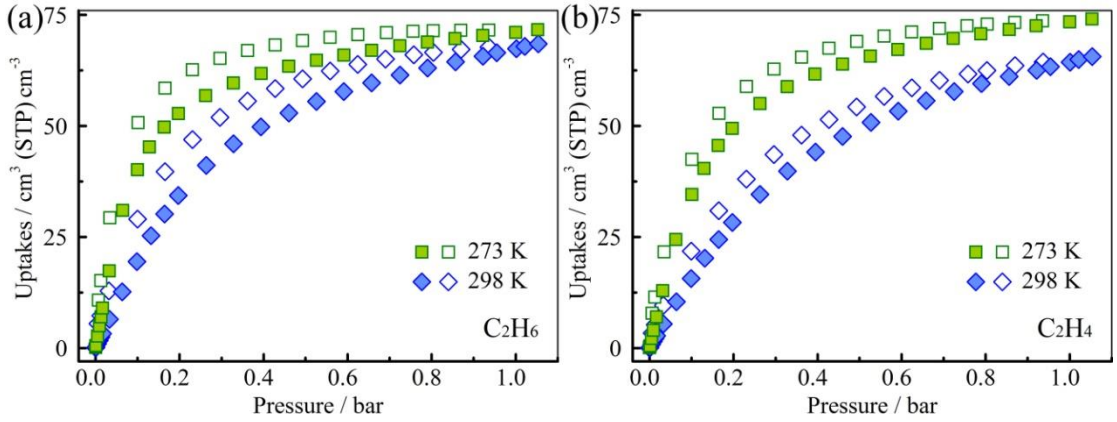

Figure S9. C_2H_6 and C_2H_4 sorption isotherms for **[Cu(ina)$_2$]** at 273 and 298 K.

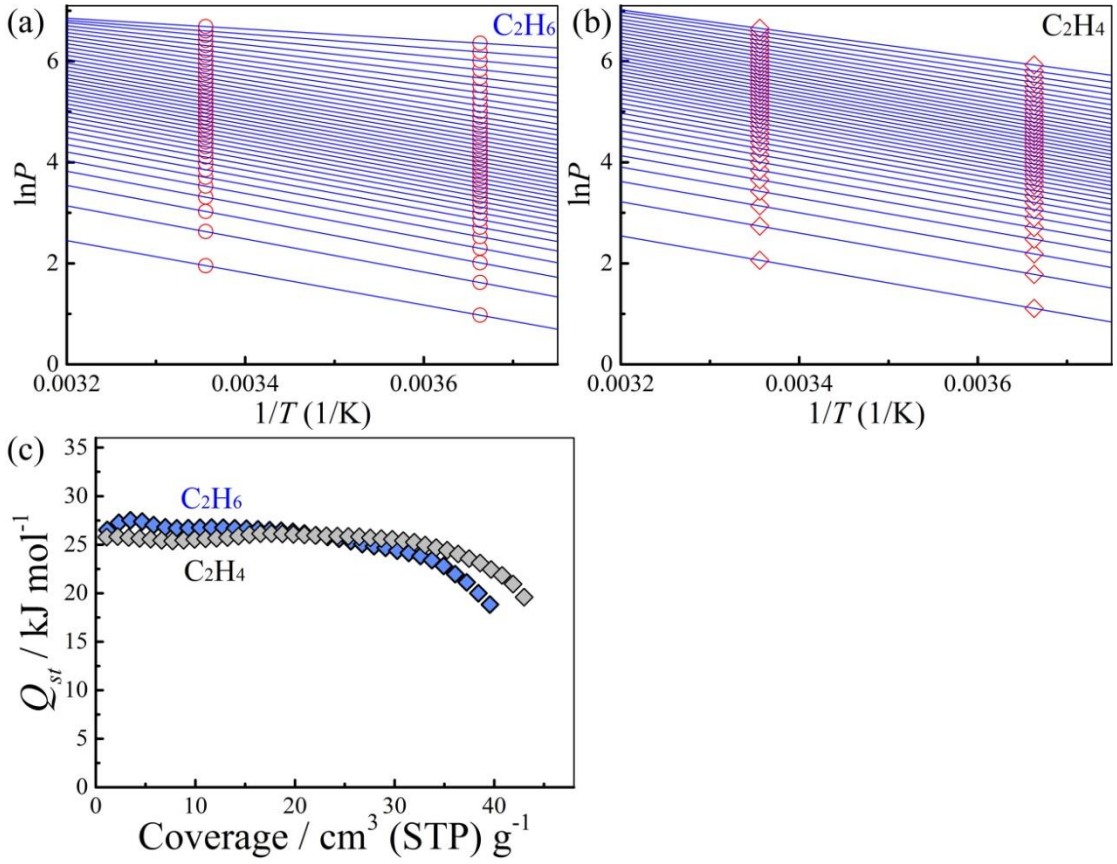

Figure S10. (a-b) Isostere plots and (c) corresponding adsorption enthalpies of **[Cu(ina)$_2$]** for C_2H_6 and C_2H_4.

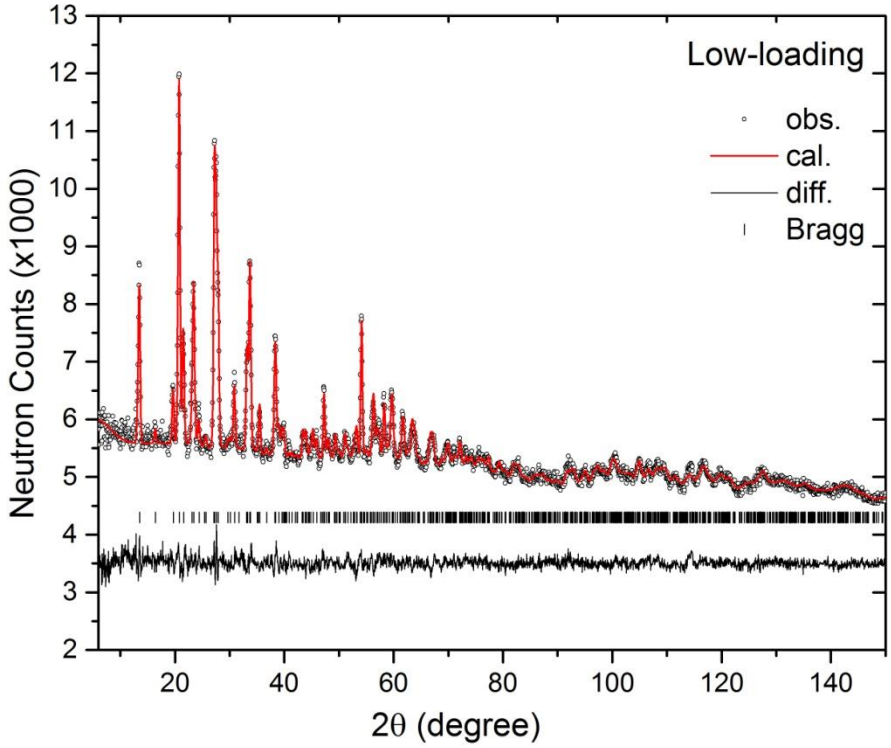

Figure S11. Neutron powder diffraction data for **[Cu(Qc)$_2$]·0.41C$_2$D$_6$** loaded with C_2D_6 (equilibrated 0.4 bar) measured at 298 K. The ligand molecules and the C_2D_6 molecules were kept as rigid bodies during the refinement. Experimental (circles), calculated (red line), and difference (black line) neutron powder diffraction profiles are shown. Vertical bars indicate the calculated positions of Bragg peaks.

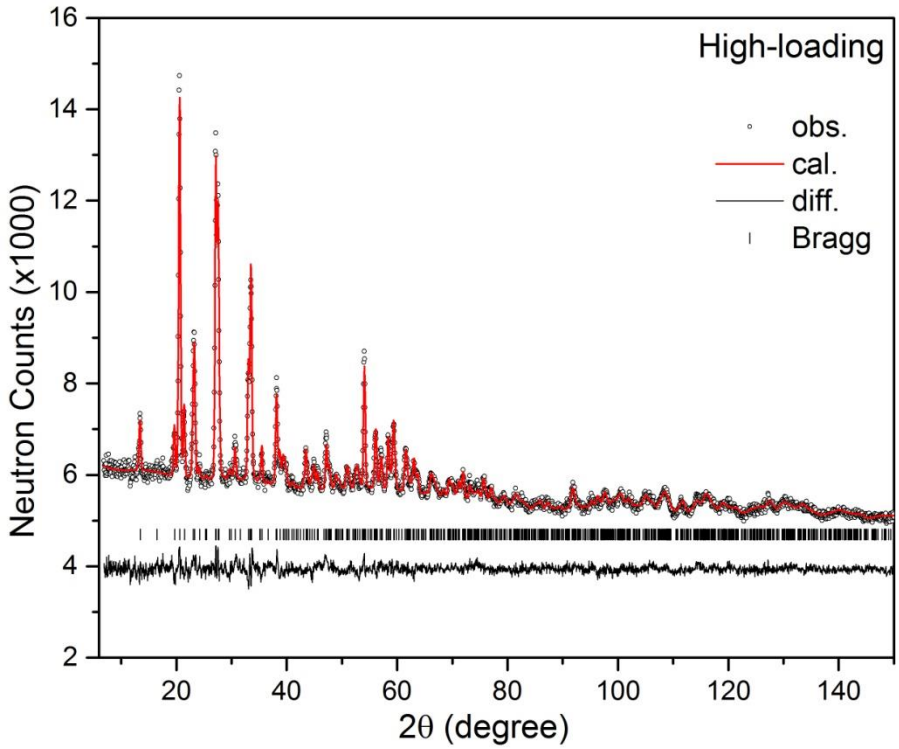

Figure S12. Rietveld refinements of the neutron powder diffraction data for **[Cu(Qc)$_2$]·0.67C$_2$D$_6$** (equilibrated 0.8 bar) measured at 298 K.

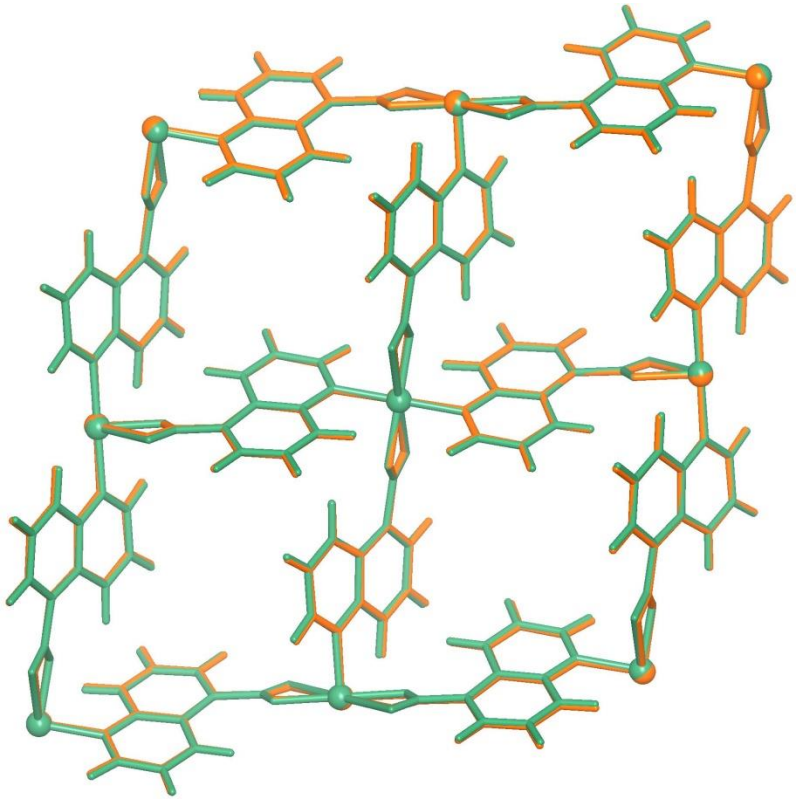

Figure S13. Conformational comparison of the framework in different C_2D_4-loading structures, bared: sea green, C_2D_4-loaded: orange. Note that no noticable structural deformation occurred.

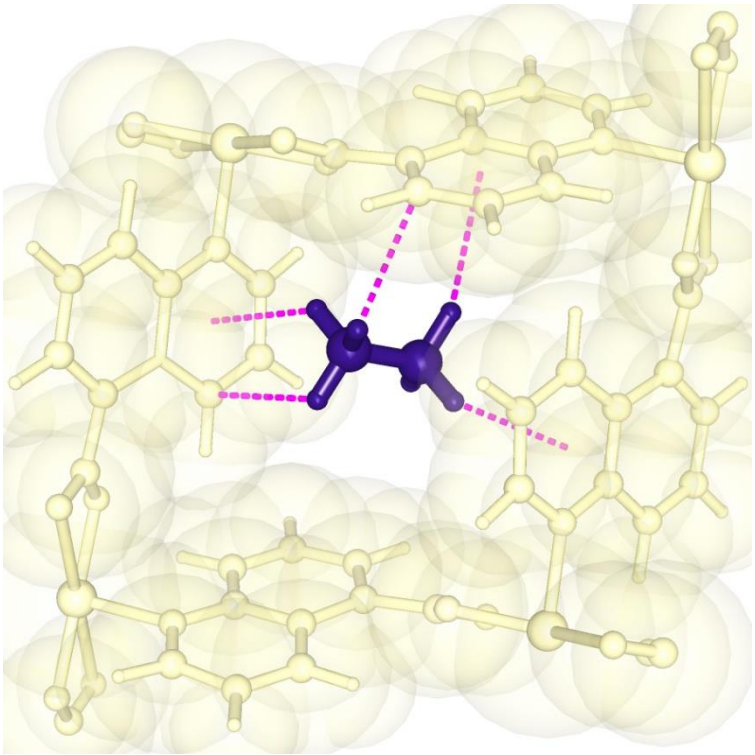

Figure S14. Neutron diffraction crystal structure of **$[Cu(Qc)_2]\cdot 0.67C_2D_6$**.

Depending on the coefficient of determination (R^2), the fitting resluts of different MOFs are presented as following:

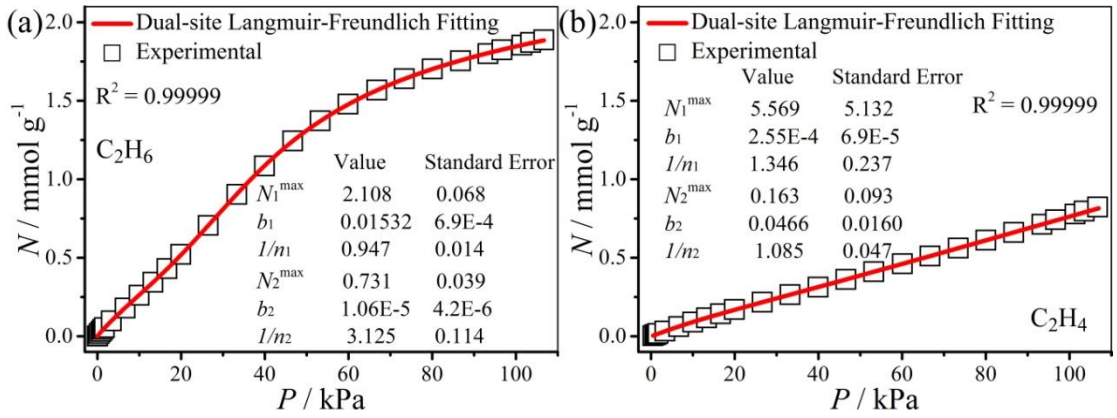

Figure S15. Dual-site Langmuir-Freundlich fitting of the C_2H_6 and C_2H_4 sorption data at 298 K and 1 bar for **Cu(Qc)$_2$** (b_1 and b_2, unit: 1/kPa).

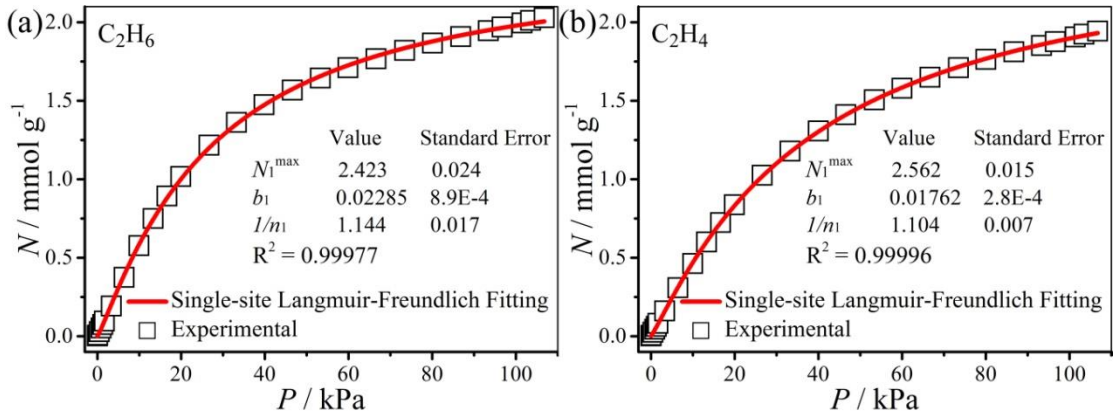

Figure S16. Langmuir-Freundlich fitting of the C_2H_6 and C_2H_4 sorption data at 298 K and 1 bar for **Cu(ina)$_2$** (b_1, unit: 1/kPa).

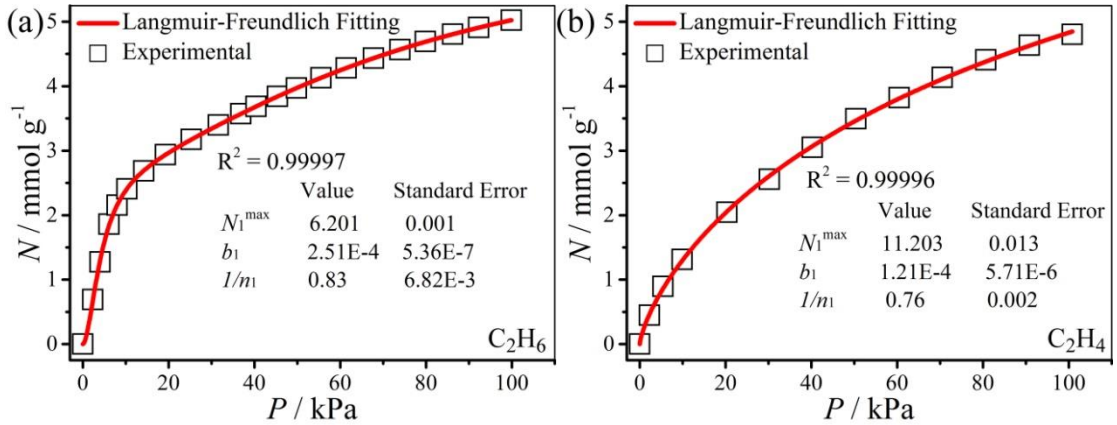

Figure S17. Langmuir-Freundlich fitting of the C_2H_6 and C_2H_4 sorption data at 298 K and 1 bar for IRMOF-8 (b_1, unit: 1/Pa).

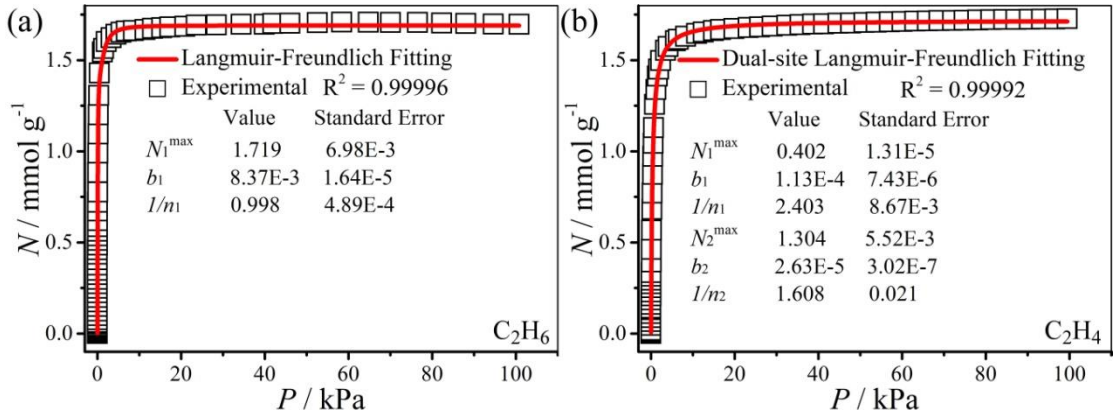

Figure S18. Langmuir-Freundlich fitting of the C_2H_6 and C_2H_4 sorption data at 298 K and 1 bar for MAF-49 (b_1 and b_2, unit: 1/Pa).

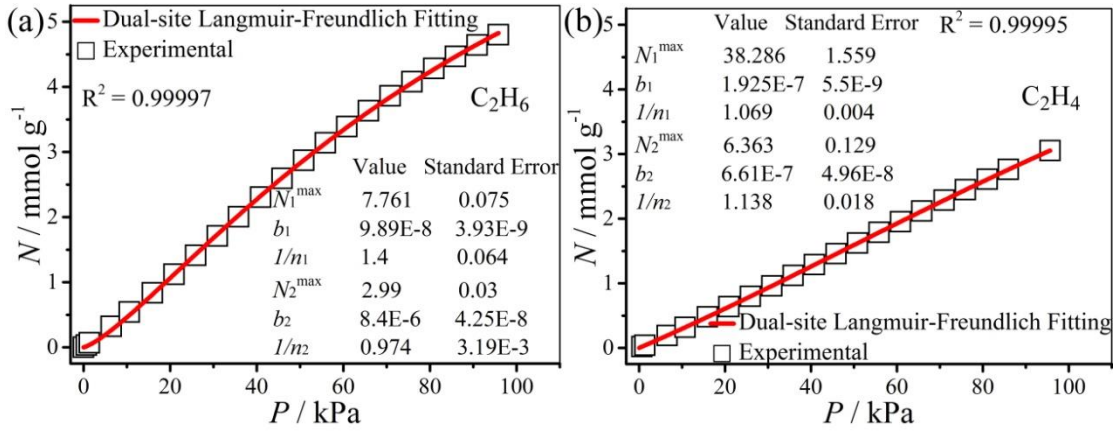

Figure S19. Dual-site Langmuir-Freundlich fitting of the C_2H_6 and C_2H_4 sorption data at 298 K and 1 bar for [Ni(bdc)(ted)$_{0.5}$] (b_1 and b_2, unit: 1/Pa).

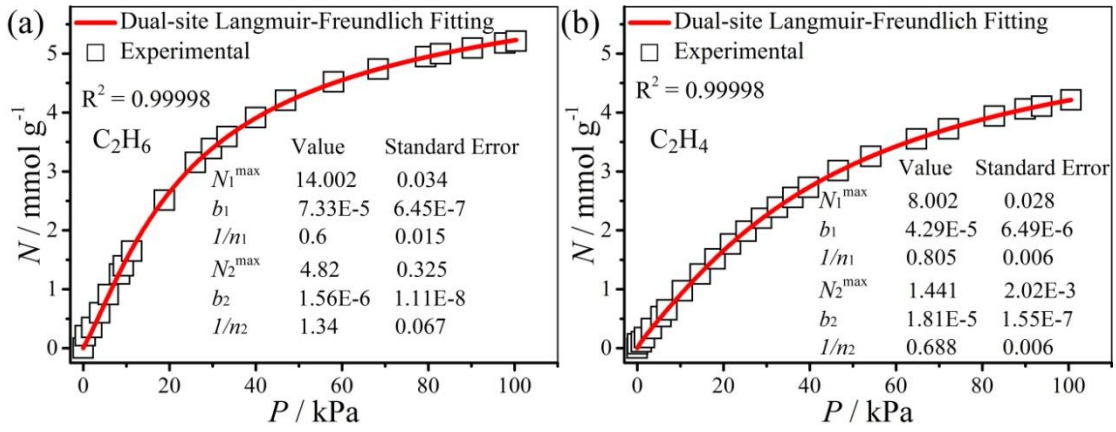

Figure S20. Dual-site Langmuir-Freundlich fitting of the C_2H_6 and C_2H_4 sorption data at 298 K and 1 bar for PCN-250 (b_1 and b_2, unit: 1/Pa).

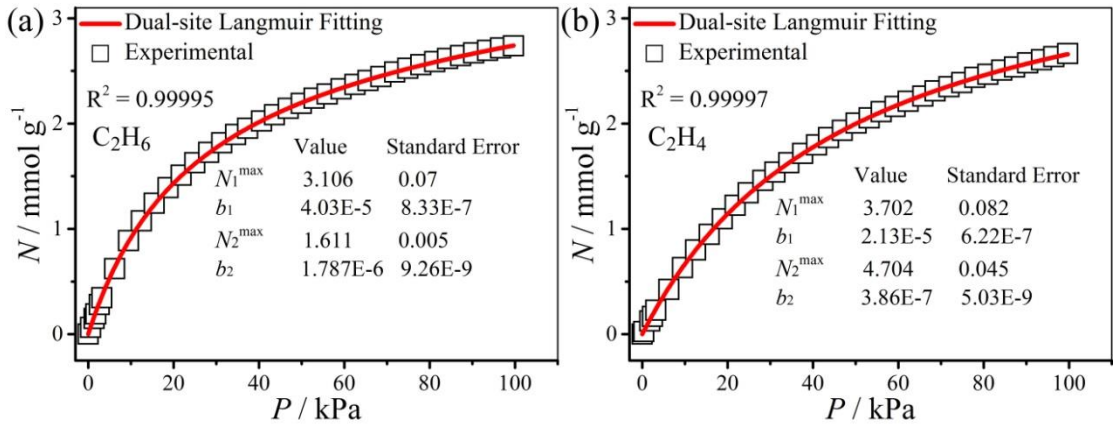

Figure S21. Dual-site Langmuir fitting of the C_2H_6 and C_2H_4 sorption data at 298 K and 1 bar for UTSA-33 (b_1 and b_2, unit: 1/Pa).

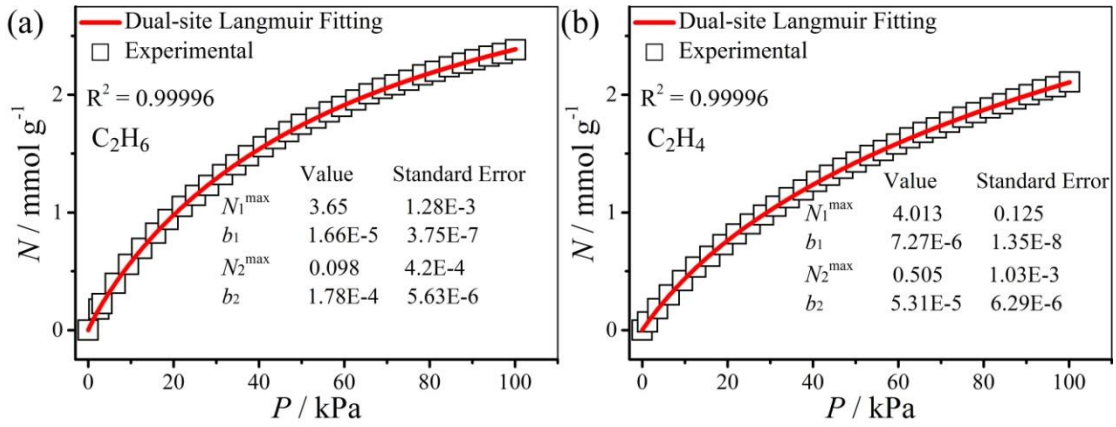

Figure S22. Dual-site Langmuir fitting of the C_2H_6 and C_2H_4 sorption data at 298 K and 1 bar for UTSA-35 (b_1 and b_2, unit: 1/Pa).

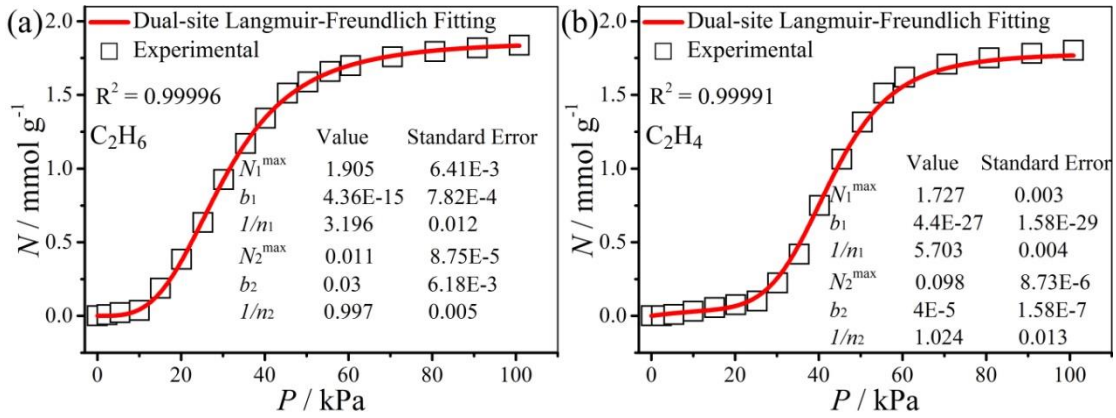

Figure S23. Dual-site Langmuir-Freundlich fitting of the C_2H_6 and C_2H_4 sorption data at 298 K and 1 bar for ZIF-7 (b_1 and b_2, unit: 1/Pa).

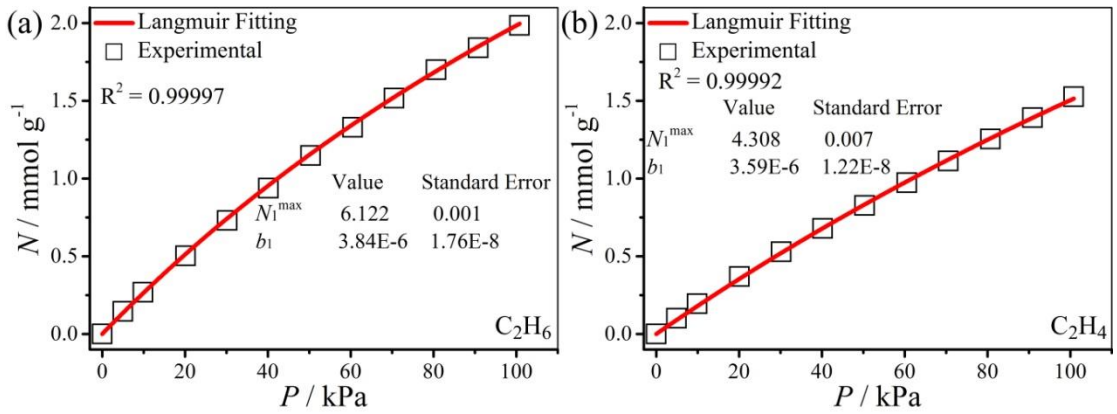

Figure S24. Langmuir fitting of the C_2H_6 and C_2H_4 sorption data at 298 K and 1 bar for ZIF-8 (b_1, unit: 1/Pa).

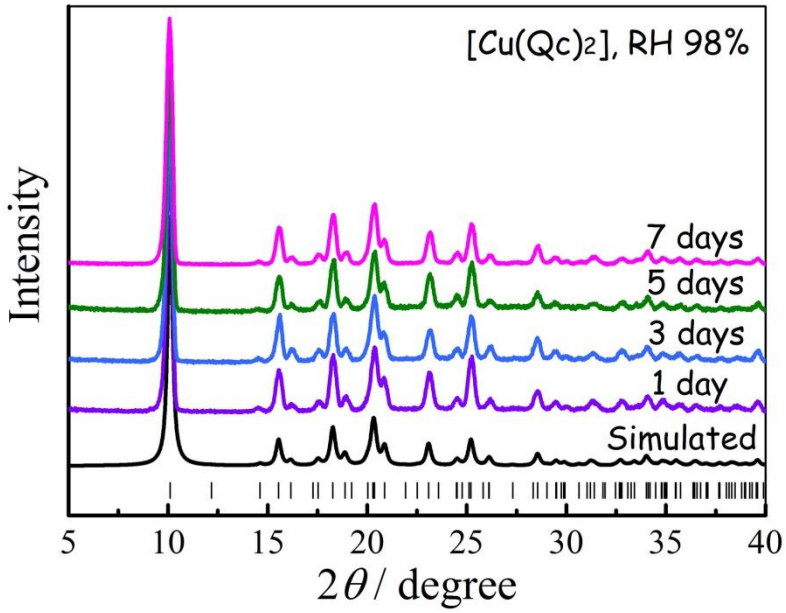

Figure S25. PXRD patterns of activated $[Cu(Qc)_2]$ after moisture exposure upon 98% relative humidity. The humidity atmosphere is controlled by saturated K_2SO_4 solution.

Table S1. Crystallographic parameters of **$[Cu(Qc)_2]\cdot 0.41C_2D_6$, $[Cu(Qc)_2]\cdot 0.16C_2D_4$, $[Cu(Qc)_2]\cdot 0.67C_2D_6$ and $[Cu(Qc)_2]$**.

Complex	**$[Cu(Qc)_2]\cdot 0.41C_2D_6$**	**$[Cu(Qc)_2]\cdot 0.16C_2D_4$**	**$[Cu(Qc)_2]\cdot 0.67C_2D_6$**	**$[Cu(Qc)_2]$**
Formula.	$C_{20.83}H_{12}D_{2.48}N_2O_4Cu$	$C_{20.31}H_{12}D_{0.62}N_2O_4Cu$	$C_{21.33}H_{12}D_{3.99}N_2O_4Cu$	$C_{20}H_{12}N_2O_4Cu$
F.W.	422.79	412.81	431.91	407.87
Crystal system	Monoclinic	Monoclinic	Monoclinic	Monoclinic
Space group	$P2_1/c$	$P2_1/c$	$P2_1/c$	$P2_1/c$
a /Å	5.7610(7)	5.6951(5)	5.8065(7)	5.6674(5)
b /Å	11.0868(13)	10.9729(13)	11.1456(11)	10.9072(12)
c /Å	14.5326(13)	14.5655(12)	14.5188(11)	14.5876(11)
β/°	94.069(7)	93.640(7)	94.423(7)	93.491(7)
volume/Å^3	925.88(21)	908.39(16)	936.81(19)	900.06(16)
Z	2	2	2	2
R_p[a] $I>2\theta$	0.0124	0.0126	0.0117	0.0138
R_{wp}[b] $I>2\theta$	0.0147	0.0150	0.0140	0.0166
GOF	1.07	0.99	1.06	1.00

[a] $R_p = \Sigma|cY^{sim}(2\theta_i) - I^{exp}(2\theta_i) + Y^{back}(2\theta_i)|/\Sigma|I^{exp}(2\theta_i)|$.

[b] $R_{wp} = \{w_p[cY^{sim}(2\theta_i) - I^{exp}(2\theta_i) + Y^{back}(2\theta_i)]^2/\Sigma w_p[I^{exp}(2\theta_i)]^2\}^{1/2}$, and $w_p = 1/I^{exp}(2\theta i)$.

Table S2. Comparison of physical parameters of C_2H_4 and C_2H_6.[S5]

	Molecular weight (g/mol)	Molecular dimensions[S6] (Å)	Boiling points (K)	Polarizability (10^{-25} cm^3)	Dipole moment (10^{-18} esu cm)	Quadruple moment (10^{-26} esu cm^2)
C_2H_4	28.05	3.3×4.2×4.8	169.4	42.5	0	1.5
C_2H_6	30.07	3.8×4.1×4.8	184.5	44.3–44.7	0	0.65

Table S3. Summary of the adsorption uptakes and selectivities for C_2H_6 and C_2H_4 in different ethane-selective MOFs (~1 bar and 298 K).

MOFs	**C_2H_6 (cm^3/g, STP)**	**C_2H_4 (cm^3/g, STP)**	**$V_{C_2H_6}/V_{C_2H_4}$ (%)**	**Selectivity**[a]	**Ref**
IRMOF-8	112.5	107.5	105	1.8	S7
MAF-49	38.7	38.0	102	2.7	S7
[Ni(bdc)(ted)$_{0.5}$]	112	76.2	147	1.6	S8
PCN-250	116.7	94.5	123	1.9	S9
UTSA-33	62.0	61.0	102	1.4	S10
UTSA-35	54.5	48.5	112	1.4	S11
ZIF-7	41.1	40.4	102	1.5	S7
ZIF-8	45.4	34.2	133	1.7	S7
Cu(ina)$_2$	*44.7*	*42.7*	*105*	*1.3*	*This*
Cu(Qc)$_2$	*41.5*	*17.5*	***237***	***3.4***	*work*

[a]All the calculations are based on the sorption data at 298 K.

Reference:

(S1) Yang, R. T. *Adsorbents: Fundamentals and Applications*; John Wiley & Sons, Inc.: Hoboken, New Jersey, 2003.

(S2) Giannozzi, P.; Baroni, S.; Bonini, N.; Calandra, M.; Car, R.; Cavazzoni, C.; Ceresoli, D.; Chiarotti, G. L.; Cococcioni, M.; Dabo, I.; Dal Corso, A.; de Gironcoli, S.; Fabris, S.; Fratesi, G.; Gebauer, R.; Gerstmann, U.; Gougoussis, C.; Kokalj, A.; Lazzeri, M.; Martin-Samos, L.; Marzari, N.; Mauri, F.; Mazzarello, R.; Paolini, S.; Pasquarello, A.; Paulatto, L.; Sbraccia, C.; Scandolo, S.; Sclauzero, G.; Seitsonen, A. P.; Smogunov, A.; Umari, P.; Wentzcovitch, R. M. *J. Phys.: Condens. Matter* **2009**, *21*, 395502.

(S3) Barone, V.; Casarin, M.; Forrer, D.; Pavone, M.; Sambi, M.; Vittadini, A. *J. Comput. Chem.* **2009**, *30*, 934.

(S4) Lin, R.-B.; Li, L.; Wu, H.; Arman, H.; Li, B.; Lin, R.-G.; Zhou, W.; Chen, B. *J. Am. Chem. Soc.* **2017**, *139*, 8022.

(S5) Li, J.-R.; Kuppler, R. J.; Zhou, H.-C. *Chem. Soc. Rev.* **2009**, *38*, 1477.

(S6) Webster, C. E.; Drago, R. S.; Zerner, M. C. *J. Am. Chem. Soc.* **1998**, *120*, 5509.

(S7) Liao, P.-Q.; Zhang, W.-X.; Zhang, J.-P.; Chen, X.-M. *Nat. Commun.* **2015**, *6*, 8697.

(S8) Liang, W.; Xu, F.; Zhou, X.; Xiao, J.; Xia, Q.; Li, Y.; Li, Z. *Chem. Eng. Sci.* **2016**, *148*, 275.

(S9) Chen, Y.; Qiao, Z.; Wu, H.; Lv, D.; Shi, R.; Xia, Q.; Zhou, J.; Li, Z. *Chem. Eng. Sci.* **2018**, *175*, 110.

(S10) He, Y.; Zhang, Z.; Xiang, S.; Fronczek Frank, R.; Krishna, R.; Chen, B. *Chem. Eur. J.* **2011**, *18*, 613.

(S11) He, Y.; Zhang, Z.; Xiang, S.; Fronczek, F. R.; Krishna, R.; Chen, B. *Chem. Commun.* **2012**, *48*, 6493.